vehicles

MDPI

Article

Numerical Investigation of Dimethyl Ether Injection Strategies in an Ammonia-Dimethyl Ether Dual-Fuel Engine

Yize Wang, Xuelong Miao *, Yage Di, Jinbao Zheng and Zhuo Yang

Department of School of Mechanical and Automotive Engineering, Shanghai University of Engineering Science, 333 Longteng Rd., Shanghai 201620, China
* Correspondence: 18909359936@163.com; Tel.: +86-18909359936

Abstract

Ammonia, as a hydrogen carrier and carbon-free alternative fuel, shows great potential in future low-carbon energy systems. This study uses dimethyl ether (DME) as a combustion promoter for ammonia to enhance the combustion performance of ammonia-fueled engines. To address the issue of unburned ammonia emissions, the original combustion chamber geometry was optimized by removing the squish area to enhance flame propagation. At an ammonia energy ratio (AER) of 60%, the modified combustion chamber (MCC) reduces unburned ammonia (uNH_3) emissions by up to 85.46% and improves indicated thermal efficiency (ITE) by 1.93% compared to the original combustion chamber (OCC). Furthermore, to achieve higher thermal efficiency and lower pollutant emissions, the DME injection strategy was redesigned based on the MCC. The results show that adjusting the single injection timing (SIT) and injection angle (INA) of DME can effectively improve the homogeneity of the in-cylinder combustible mixture and enhance combustion efficiency; however, overly concentrated injection can lead to rapid heat release and increase the risk of knock. The split injection strategy enables more controllable combustion phasing, significantly reduces the maximum pressure rise rate (MPRR) and ringing intensity (RI), and mitigates knocking tendency. When the main injection timing (MIT) is −5 °CA ATDC, pilot injection timing (PIT) is −30 °CA ATDC, and the pilot injection ratio (PIR) is 60%, the ITE reaches 49.98%, which is 3.53% higher than that of the pure diesel mode. Greenhouse gas (GHG) and NO_x emissions are reduced by 45.94% and 62.49%, respectively, with uNH_3 emissions as low as 4.16 g/kW·h.

Keywords: ammonia–dimethyl ether dual-fuel engines; combustion chamber geometry; injection strategy; indicated thermal efficiency; greenhouse gas

Check for updates

Academic Editor: Dariusz Szpica

Received: 9 July 2026
Revised: 8 August 2026
Accepted: 12 August 2026
Published: 24 August 2026

Copyright: © 2026 by the authors. Licensee MDPI, Basel, Switzerland. This article is an open access article distributed under the terms and conditions of the Creative Commons Attribution (CC BY) license.

1. Introduction

In response to the energy transition and carbon neutrality goals, the development of low-/zero-carbon fuels and high-efficiency clean combustion strategies has become a key focus in the field of internal combustion engine research. Hydrogen has excellent combustibility and low ignition energy, and its complete combustion yields only water, meeting the requirements of low-carbon and environmentally friendly combustion. As a result, it has attracted widespread attention in the combustion research community [1]. However, hydrogen as a fuel still faces numerous challenges in production, storage, and transportation [2]. In contrast, ammonia, another carbon-free clean energy source, is considered a more promising carbon-neutral fuel due to its high energy density, ease of liquefaction, low production cost, and convenient storage and transportation. However,

the slow combustion speed and low reactivity of ammonia present significant challenges when used as a sole fuel in engines [3]. To improve the combustion characteristics of NH_3 and achieve stable and efficient combustion in compression ignition (CI) engines, reactive additives are commonly introduced to enhance its reactivity. In recent years, extensive research has been conducted on ammonia co-firing with various fuels.

Wen et al. [4] experimentally mixed ammonia with biomass-derived syngas (biosyngas) to enhance its reactivity and analyzed the reaction pathways of NH_3 to reduce NO_x emissions. Shrestha et al. [5] found that increasing the hydrogen content or enriching the oxygen concentration in the mixture can effectively enhance the laminar burning velocity, with the effect of adding 9% oxygen being equivalent to that of adding 30% hydrogen. Okafor et al. [6] extensively measured the laminar burning velocity of NH_3/CH_4 mixtures under high pressure and found that the velocity decreases with increasing ammonia concentration and pressure.

As shown in Table 1 [7–9], compared to other fuels, dimethyl ether (DME) is a clean fuel second only to hydrogen, with a high cetane number and diverse sources, making it an excellent fuel additive [10].

Table 1. The fuel properties.

Properties	NH_3	Diesel	H_2	DME
Lower heating value (MJ/kg)	18.8	45	120	28.8
Autoignition temperature (K)	923	530–560	775–850	508
Flammability limit (vol, %)	15–28	0.6–5.5	4–75	3.4–17
Adiabatic flame temperature (°C)	2073	2400	2383	1920
Laminar flame speed at φ = 1 (cm/s)	7	86	290–350	28–35
Stoichiometric air–fuel ratio (/)	6.03	14.5	34.3	9.0

In addition, another advantage of DME is that it is non-toxic, non-mutagenic, and non-carcinogenic, with an extremely short atmospheric lifetime of less than one week and a global warming potential (GWP) as low as approximately 1 [11,12]. Gross C.W. [13] and Ryu K. [14] experimentally demonstrated that blending DME significantly promotes the combustion of ammonia fuel. However, under lean combustion and high ammonia energy ratio conditions for emission control, the ignition timing becomes increasingly difficult to stabilize, leading to poorer combustion consistency. Li et al. [15] used numerical simulations to investigate the effects of ammonia energy ratio (AER), DME injection timing, and ammonia injection pressure on the performance of a direct-injection ammonia/DME marine engine. The results showed that advancing the DME injection timing appropriately and increasing the liquid ammonia injection pressure can effectively reduce NO_x emissions and improve thermal efficiency.

It is worth noting that in-cylinder direct injection of ammonia faces challenges such as ignition difficulty, unstable combustion, and complex injection systems [16], making it difficult to achieve efficient and reliable combustion. In contrast, introducing ammonia through the intake port allows the formation of a well-premixed charge, which helps stabilize combustion and simplifies system design. However, introducing ammonia via the intake manifold can lead to significant fuel slip, resulting in severely reduced combustion efficiency. Moreover, as a toxic gas, ammonia poses a serious risk to human health and life when its concentration exceeds 300 ppm [17]. In internal combustion engine design, an appropriately shaped combustion chamber can significantly enhance combustion quality [18]. This is particularly important for ammonia, which has low reactivity; optimizing the combustion chamber shape based on dual-fuel combustion processes and flame propagation paths is considered one of the most effective strategies to reduce unburned am-

monia emissions [19,20]. In addition, optimizing the injection strategy can further reduce pollutant emissions and improve thermal efficiency [21].

Liu et al. [22] employed numerical simulations and a genetic algorithm to perform multi-objective parametric study of the combustion chamber geometry (CCG) in a diesel/natural gas dual-fuel engine. The results showed that a straight-line combustion chamber could effectively reduce CH_4 emissions, achieving an indicated thermal efficiency (ITE) as high as 50.2% when the injection timing was set to −16.45 °CA ATDC. Ye et al. [23] investigated the effects of several common CCGs on combustion and flame propagation characteristics in ammonia–diesel dual-fuel (ADDF) engines. They found that stronger reverse squish enhanced fuel diffusion in the squish regions of the original combustion chamber (OCC), petal-type combustion chamber (PTCC), and shallow-depth combustion chamber (SCC). In the case of the toroidal combustion chamber (TCC), stronger swirl motion significantly improved diffusion combustion. Shi et al. [24] calibrated their simulation model based on the experimental data from Yousefi et al., and then optimized the diesel injection timing and injection angle at a 40% ammonia energy ratio (AER) to improve thermal efficiency. The optimal configuration reduced unburned ammonia emissions to as low as 0.279 g/kw·h. However, the stability and reliability of the engine under actual operating conditions have not been fully considered. Similarly, Shin et al.optimized diesel injection timing under various AERs and showed that, compared with the pure diesel mode, advancing the injection timing at high AER significantly reduced greenhouse gas (GHG) emissions by up to 80.6%. Mi et al. [25] experimentally demonstrated that a split injection strategy enables stable combustion and GHG reduction over a wide AER range in ADDF engines; however, it inevitably leads to higher NO_x, CO, and unburned hydrocarbon (uHC) emissions.

In summary, employing ammonia introduced through the intake port combined with direct injection of DME into the cylinder in a CI engine can fully leverage ammonia's zero-carbon emissions and DME's low-carbon, high-reactivity advantages as a mixed fuel. However, current research on ammonia/DME dual-fuel combustion primarily emphasizes fundamental combustion characteristics and chemical kinetics, while studies that explore the adaptation of injection strategies to specific combustion chamber geometries remain scarce. In a recent study [26], we optimized the original combustion chamber geometry under the ADME-DF mode based on dual-fuel combustion characteristics by eliminating the squish region to enhance flame propagation, aiming to reduce unburned ammonia (uNH_3) and greenhouse gas (GHG) emissions while improving combustion efficiency.

Furthermore, to fully unlock the potential of the modified combustion chamber (MCC), comparative analyses show that the MCC yields a maximum 85.46% reduction in unburned ammonia (uNH_3) emissions and a 1.93% improvement in indicated thermal efficiency (ITE) compared with the original combustion chamber (OCC). Nevertheless, as no matching adjustments to the injection strategy have been developed for the redesigned chamber geometry, its combustion and emission performance deteriorates below that of the OCC at elevated ammonia energy ratios (AERs).

To address this limitation, the present study optimizes the dimethyl ether (DME) injection strategy tailored to the modified combustion chamber architecture. Four key parameters are systematically investigated: injector inclination angle (INA) and single injection timing (SIT) for the single-injection scheme, as well as pilot injection timing (PIT) and pilot injection ratio (PIR) for the split-injection scheme. This work aims to further curb uNH_3 and greenhouse gas (GHG) emissions under the ammonia–dimethyl ether dual-fuel (ADME-DF) mode, while sustaining stable engine operation and attaining high thermal efficiency.

2. Materials and Methods

2.1. Model Development

The engine model used in this study is a four-stroke, single-cylinder compression ignition (CI) engine, with the basic parameters listed in Table 2. Given the 7-hole injector with nozzle holes symmetrically distributed about the cylinder centerline, a 1/7 sector computational domain was established using periodic boundary conditions. This approach significantly reduces the mesh size and computational cost while fully retaining the physical properties of the in-cylinder flow field and combustion process.

Table 2. Engine specifications.

Specification	Unit	Value
Engine model	-	DK 32
Number of cylinders	-	1
Bore × Stroke	mm	113 × 140
Total displacement	L	1.404
Compression ratio	-	17.5:1
Rated power	kW	23.53
Combustion chamber	-	ω
Number of spray holes	-	7
Nozzle hole diameter	mm	0.19
Intake valve closing (IVC)	°CA ATDC	−169.7
Exhaust valve opening (EVO)	°CA ATDC	145.3

A constant-volume initialization scheme was employed, and the intricate geometry of the intake and exhaust ports was omitted from the model. As the computational domain spans the closed cycle from intake valve closing (IVC) to exhaust valve opening (EVO), the simulations focus on in-cylinder compression, fuel injection, combustion and expansion processes, with flow losses in the intake and exhaust ports excluded from consideration.

For the intake process, it is assumed that ammonia delivered via low-pressure port injection is fully and homogeneously premixed with in-cylinder air at the molecular level at IVC. Furthermore, the in-cylinder gas is treated as an ideal gas, and isothermal boundary conditions are applied to all solid walls including the cylinder head, cylinder liner and piston crown. The key boundary conditions used in the simulations are summarized in Table 3.

Table 3. Boundary conditions.

Parameter	Value
In-cylinder pressure at intake valve closing (MPa)	0.11
In-cylinder temperature at intake valve closing (K)	340
Piston crown temperature (K)	500
Cylinder liner temperature (K)	460
Cylinder head temperature (K)	500
Swirl ratio	1.2
DME injection pressure (MPa)	30
Engine speed (r/min)	1200
Torque (N·m)	109.4

The RNG k-ε model [27] was employed to predict the complex in-cylinder turbulence. The KH-RT model [28] was used to characterize the primary and secondary breakup of spray droplets, while the Frossling model [29] was applied to simulate droplet evaporation. The NTC model [30] was adopted to model droplet collisions. Wall heat transfer was calculated using the model developed by O'Rourke and Amsden [31]. All three-dimensional

CFD simulations presented in this work are carried out using the commercial CONVERGE 3.0 software package. Featuring built-in capabilities for adaptive mesh refinement, detailed chemical kinetic solving, and spray-wall interaction modeling, this software aligns perfectly with the numerical methodology adopted in this study.

Furthermore, the model provides a complete representation of droplet adhesion, rebound and splash upon wall impingement. The fate of impinging droplets is determined by the incident Weber number and wall boundary conditions, and the formulation is capable of capturing the formation, spreading and transport of wall liquid films. It also accurately reproduces the evaporation characteristics of DME associated with its high volatility, laying a robust physical basis for investigations into mixture formation and combustion processes.

The in-cylinder combustion process is computed using the SAGE detailed chemical kinetics solver [32]. The detailed NH_3/DME reaction mechanism adopted in this study incorporates a comprehensive nitrogen chemistry network, which allows direct resolution of the concentration evolution of all nitrogen-bearing species—including NO, NO_2, N_2O and unburned ammonia—eliminating the need for an additional standalone NO_x formation model. This mechanism accounts for both the Zeldovich pathway governing thermal NO formation at elevated temperatures and complete nitrogen reaction channels involving fuel-NO_x and N_2O intermediates throughout the ammonia oxidation process. The sub-models implemented in the numerical simulations are listed in Table 4. The selection of an appropriate combustion mechanism plays a critical role in numerical investigations of engine combustion. The comprehensive detailed mechanism for ammonia/DME combustion developed by Yin et al. [33], based on the mechanisms proposed by Hashemi et al. [34] and Zhang et al. [35], includes 193 species and 1669 reactions. The core nitrogen chemistry sub-mechanism governing ammonia oxidation in the adopted mechanism has been calibrated against species concentration measurements from jet-stirred reactor experiments. Its predictive accuracy for the concentration evolution of key nitrogen-bearing species, including NO and N_2O, has been experimentally validated across wide ranges of temperature and equivalence ratio. Over a broad operating envelope spanning 298–423 K and 1–5 atm, the mechanism yields prediction errors within 10% for both the laminar flame speed and high-pressure ignition delay of NH_3/DME mixtures. It accurately reproduces the reaction pathways and NO_x formation characteristics during dual-fuel combustion, providing a robust kinetic basis for numerical simulations of in-cylinder combustion and emission processes.

Table 4. Sub-models used in the simulation.

Models	Name
Turbulence model	RNG k-ε
Break-up model	KH-RT
Wall heat transfer and spray-wall interaction model	O'Rourke and Amsden
Drop evaporation model	The Frossling correlation
Collision model	NTC
Combustion model	SAGE
NO_x emission	computed via SAGE solver with detailed chemical kinetics

Direct solution of nitrogen-containing emissions coupled with detailed chemical kinetic mechanisms is a widely accepted practice in three-dimensional CFD studies of ammonia dual-fuel engines [36]. In the absence of direct engine test data, employing a stepwise

validation strategy is a well-established and widely accepted standard practice in CFD literature [37].

Simulations are performed with an adaptive time-stepping scheme governed by a Courant–Friedrichs–Lewy number of 0.7 and a maximum allowable crank angle step of 0.5 °CA [38]. Convergence at each time step is achieved when the residuals for the continuity and momentum equations fall below 1×10^{-4}, those for the energy and species transport equations drop below 1×10^{-6}, and the relative variations in mean in-cylinder pressure and temperature across three consecutive iterations remain within 0.1% [25,39]. Adaptive mesh refinement is applied based on gradient thresholds of 200 K for temperature, 50 m/s for velocity, and 0.1 for both DME and NH_3 mass fractions. Three levels of fixed embedding are imposed on the core fuel injection region, resulting in a local minimum cell size of 0.25 mm, and a global lower limit of 0.125 mm is enforced for all cells to avoid excessive mesh refinement [24,40].The main boundary conditions used in the simulation are summarized in Table 5. To sufficiently reduce unburned ammonia emissions, the equivalence ratio is set to 1.2. A conventional trapezoidal injection rate profile is applied for DME injection, with an injection duration of 10 °CA and a spray cone angle of 10°.

Table 5. Computational boundary conditions.

Parameters	Unit	Value
Injection pressure (DME)	bar	300
Injection duration	°CA	10
Injection rate profile	-	Trapezoidal
Spray cone angle	°	12
Fuel temperature (DME)	K	340
Initial turbulence kinetic energy (k)	m^2/s^2	62.0271
Initial turbulence dissipation rate (ε)	m^2/s^3	17,183.4
Global Equivalence Ratio (ϕ)	-	1.2
Speed	rpm	1200
IVC pressure	bar	1.2
IVC temperature	K	340
Piston temperature	K	500
Wall temperature	K	460
Head temperature	K	500
Swirl ratio	-	1.2

2.2. Definition of Relevant Characteristic Parameters

In this study, the apparent heat release rate (AHRR) was calculated using cylinder volume and in-cylinder pressure according to Equation (1), where P is the in-cylinder pressure, V is the cylinder volume, θ is the crank angle, and γ is the ratio of specific heats.

$$\mathrm{AHRR} = \frac{\gamma}{\gamma - 1} \mathrm{P} \frac{\mathrm{dV}}{\mathrm{d}\theta} + \frac{1}{\gamma - 1} \mathrm{V} \frac{\mathrm{dP}}{\mathrm{d}\theta} \quad (1)$$

CA10, CA50, and CA90 correspond to the crank angle positions at which 10% (start of combustion), 50% (location of heat release centroid), and 90% (end of combustion) of the cumulative heat release from in-cylinder dual-fuel combustion occurs, respectively. The ignition delay and combustion duration are defined as the time intervals SOI–CA10 and CA10–CA90, respectively.

The ammonia energy ratio (AER) is calculated according to Equation (2), where AER denotes the proportion of energy contributed by ammonia. F_{mNH_3} represents the total mass of ammonia injected per cycle, F_{mDME} denotes the mass of dimethyl ether (DME)

injected per cycle, and LHV_{DME} and LHV_{NH_3} are the lower heating values of DME and ammonia, respectively.

$$\text{AER}\ (\%) = \frac{Fm_{NH_3} \times LHV_{NH_3}}{Fm_{DME} \times LHV_{DME} + Fm_{NH_3} \times LHV_{NH_3}} \times 100\% \quad (2)$$

The formulas for calculating indicated thermal efficiency (ITE) and unburned energy losses are given by Equations (3) and (4), respectively. In these equations, W_i refers to the indicated work per engine cycle. m_{NH_3}, m_{DME}, m_{HC} and m_{CO} represent the masses of unburned NH_3, DME, HC, and CO, respectively. LHV_{HC} and LHV_{CO} denote the lower heating values of HC and CO, respectively.

$$\text{ITE}\ (\%) = \frac{W_i}{Fm_{DME} \times LHV_{DME} + Fm_{NH_3} \times LHV_{NH_3}} \times 100\% \quad (3)$$

$$\text{Unburned Loss}\ (\%) = \frac{m_{DME} \times LHV_{DME} + m_{NH_3} \times LHV_{NH_3} + m_{HC} \times LHV_{HC} + m_{CO} \times LHV_{CO}}{Fm_{DME} \times LHV_{DME} + Fm_{NH_3} \times LHV_{NH_3}} \times 100\% \quad (4)$$

Greenhouse gas (GHG) emissions are quantified on a CO_2-equivalent mass basis, accounting for both CO_2 and N_2O species formed during in-cylinder combustion, and are calculated according to the following equation:

$$GHG\ = m_{CO_2} + m_{N_2O} \times GWP_{N_2O} \quad (5)$$

where m_{CO_2} denotes the mass of CO_2 emissions, m_{N_2O} denotes the mass of N_2O emissions, and GWP_{N_2O} is the global warming potential of nitrous oxide. In this work, a value of 298 is adopted for N_2O, as specified in the Fifth Assessment Report of the Intergovernmental Panel on Climate Change over a 100-year time horizon, while the baseline GWP of CO_2 is taken as unity.

A specific resonant frequency generated within the cylinder produces high-intensity pressure waves, referred to as ringing intensity (RI), which can be used to evaluate the engine's knocking tendency [41]. RI reflects the maximum pressure rise rate (MPRR) and can be calculated using Equation (5), where γ is the ratio of specific heats; $\left(\frac{dp}{dt}\right)_{max}$ represents the engine's maximum pressure rise rate (MPRR); R is the universal gas constant; and β is a coefficient derived from pressure oscillations, typically taken as 0.05 ms. P_{max} and T_{max} denote the maximum in-cylinder pressure and temperature, respectively.

$$RI = \frac{\sqrt{\gamma R T_{max}}}{2\gamma P_{max}} \left[\beta \left(\frac{dP}{dt}\right)_{max}\right]^2 \quad (6)$$

This study adopts the standard knock evaluation limits widely used in internal combustion engine research: a maximum pressure rise rate (MPRR) of 1.2 MPa/°CA [42] and a ringing intensity (RI) of 5 MW/m^2 [43] are defined as the safe thresholds, beyond which the knocking tendency is considered unacceptable.

A multi-objective trade-off criterion is therefore formulated: with MPRR and RI strictly constrained within the safe allowable limits (1.2 MPa/°CA and 5 MW/m^2, respectively), the parametric study seeks to maximize the indicated thermal efficiency (ITE) while simultaneously minimizing unburned ammonia and greenhouse gas emissions.

All pollutant and greenhouse gas emissions reported throughout this study, given in units of g/kW·h, represent indicated specific emissions and are thus evaluated on the same basis as indicated thermal efficiency. The indicated specific emissions are derived from the

mass of exhaust pollutants per engine cycle and the indicated work per cycle, as defined by the following equation:

$$\left(e_i = \frac{m_{emission} \times 3600}{W_i}\right) \quad (7)$$

where e_i denotes the indicated specific emission in g/kW·h, $m_{emission}$ represents the mass of the corresponding pollutant emitted per engine cycle in grams, W_i is the indicated work per cycle in joules, and the coefficient 3600 is employed for unit conversion.

2.3. Model Validation

To ensure the numerical reliability of the three-dimensional CFD model, general fluid dynamic and numerical submodels are calibrated against well-established experimental data from a diesel engine, while a detailed chemical kinetic mechanism validated against fundamental combustion measurements is adopted to guarantee the accuracy of dual-fuel combustion simulations.

The validation under pure diesel operation covers general computational modules including the RNG k-ε turbulence model, the KH-RT spray breakup model, droplet evaporation and collision models, the wall heat transfer model, as well as grid resolution and numerical solution schemes. The predictive accuracy of these submodels is not inherently dependent on fuel type, as they constitute the foundational components of internal combustion engine CFD simulations. Calibration against baseline diesel operation is standard practice in the field, and ensures reliable computation of in-cylinder flow fields, spray development, and heat transfer processes.

For ammonia–dimethyl ether dual-fuel combustion, the detailed kinetic mechanism developed by Yin et al.is employed in this work. This mechanism has been comprehensively validated against multiple sets of fundamental combustion measurements, including laminar flame speeds and species profiles from jet-stirred reactor experiments across wide temperature and pressure ranges. It delivers reasonable prediction errors for global combustion characteristics and offers good accuracy in capturing the concentration evolution of key nitrogen-containing species such as NO and N_2O, thereby providing a robust kinetic foundation for numerical investigations of dual-fuel in-cylinder combustion and exhaust emissions.

To ensure the accuracy of the CFD simulation results, the present study validated the model using experimental data for pure diesel combustion reported by Jin et al. [44]. The surrogate diesel mechanism was based on the n-dodecane skeletal mechanism developed by Frassoldati et al. [45], which includes 96 species and 993 reactions. A grid independence study was performed prior to the full simulation matrix. As illustrated in Figure 1a, four base mesh sizes were examined to evaluate their impact on in-cylinder pressure predictions. The results show that the pressure trace obtained with the 2.8 mm mesh exhibits noticeable discrepancies. In contrast, no appreciable differences are observed among the results computed with mesh sizes of 1.6 mm, 2.0 mm and 2.4 mm. Accordingly, a base mesh size of 2.0 mm was selected to strike a reasonable balance between computational accuracy and numerical efficiency.

Figure 1b,c compare the simulated and experimental in-cylinder pressure and heat release rate (HRR). The simulated in-cylinder pressure agrees well with the experimental data, while some discrepancies are observed in the HRR curves. These differences are primarily attributed to the use of a sector mesh model [46], as well as variations in cetane number and heating value between real diesel and n-dodecane. Additionally, the application of isothermal wall boundary conditions in the simulations leads to deviations in wall heat transfer losses relative to real engine conditions, and further accounts for the overprediction of the peak heat release rate compared with experimental measurements [47]. Figure 1d presents

a comparison of key pollutant emissions, with all discrepancies remaining within 8.5%. In summary, the developed simulation model is reliable and provides a solid foundation for future studies on engine performance parametric study and emission control strategies.

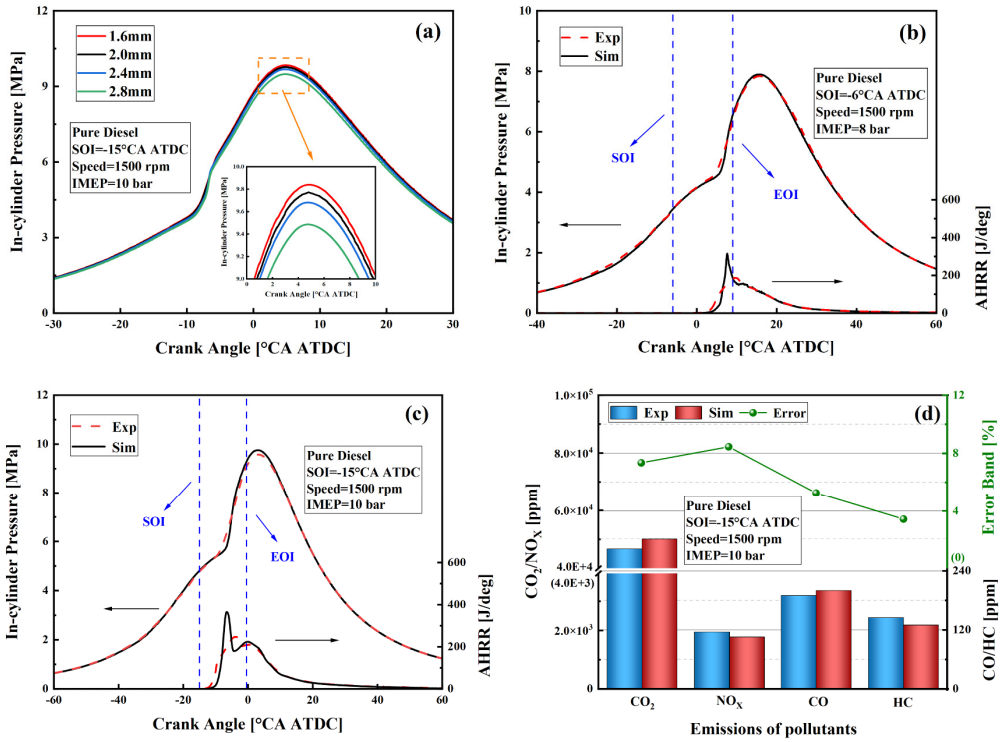


Figure 1. Model validation: (**a**) grid independence verification; (**b**,**c**) in-cylinder pressure and AHRR; (**d**) major emissions.

2.4. Selected Simulation Cases

The geometry of the combustion chamber significantly influences in-cylinder flow characteristics and flame propagation, particularly in ADME-DF engines. To enhance combustion efficiency and reduce pollutant emissions, the combustion chamber geometry (CCG) should be optimized based on the properties of the fuels and the combustion process. As shown in Figure 2c, for the original combustion chamber (OCC), a squish region is formed between the piston crown and cylinder head when the piston reaches top dead center (TDC). This squish region adversely affects the distribution of ammonia fuel and flame propagation in the cylinder, thereby reducing combustion efficiency and increasing emissions. To mitigate these issues, this study proposes a modification to the OCC. The squish region is removed while maintaining the same combustion chamber volume, aiming to improve flame propagation and reduce uNH_3 emissions.

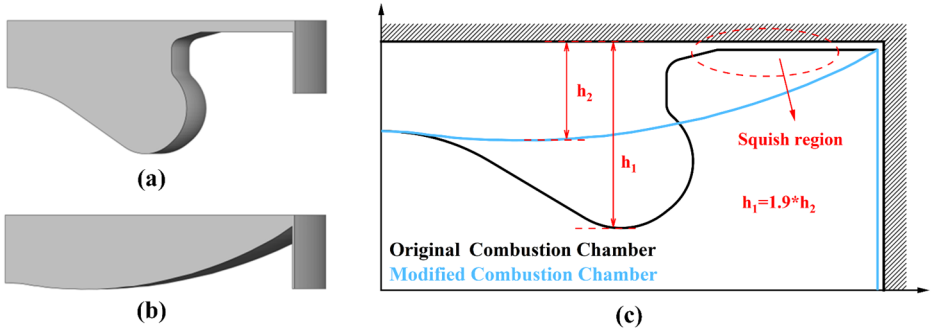


Figure 2. Combustion chamber geometries: (**a**) OCC; (**b**) MCC; (**c**) comparison of CCGs.

Due to the influence of combustion chamber geometry on mixture formation, flame propagation, and the local combustion environment, an optimized injection strategy is necessary to achieve more complete combustion, higher thermal efficiency, and lower emissions. In addition, when DME is used as an alternative fuel in CI engines, its lower heating value and density compared to diesel typically require increasing the injection pressure, nozzle diameter, or the number of nozzle holes. However, using a small amount of DME can also simplify the modification of fuel injection systems [48,49]. Therefore, in this study, based on the MCC, a constant DME injection pressure of 300 bar and an AER of 60% were adopted. For the single injection strategy, the injection nozzle angle (INA) was varied from 55° to 85°, and the single injection timing (SIT) was varied from −35 °CA ATDC to −10 °CA ATDC. For the split injection strategy, the main injection timing (MIT) was fixed at −5 °CA ATDC, while the pre-injection ratio (PIR) was varied from 20% to 80%, and the pre-injection timing (PIT) from −70 °CA ATDC to −30 °CA ATDC. The effects of injection strategies on the performance of the ADME-DF engine were systematically investigated. Detailed injection strategies are shown in Table 6.

Table 6. Case parameters used in the simulation.

Test No.	DME Injection Strategy	Parameters	Value
-	-	NH3 fuel injection	98 mg/cyc PFI @ 60%AER
-	-	DME fuel injection	42 mg/cyc DI @ 300bar
1	Single injection	DME injection nozzle angle (INA)	55°/65°/75°/80°/85°
		DME single injection timing (SIT)	−35/−30/−25/−20/−15/−10 °CA ATDC
2	Double injection	DME main injection timing (MIT)	−5 °CA ATDC
		DME pre-injection timing (PIT)	−30/−40/−50/−60/−70 °CA ATDC
		DME pre-injection ratio (PIR)	20%/40%/60%/80%

3. Results and Discussion

3.1. Effects of AER and CCG on the Performance of ADME-DF Engines

The effects of Ammonia Energy Ratio (AER) and Combustion Chamber Geometry (CCG) on the ADME-DF engine have been investigated in our previous work, and are revisited here for completeness. Figure 3a,b compare in-cylinder pressure, HRR, and combustion phasing under different AERs for the OCC and MCC. It can be observed that the combustion characteristics under varying AERs are similar for both CCGs. Specifically, the P_{max} decreases with increasing AER, while the peak HRR initially increases and then decreases, reaching its maximum at an AER of 60%. The gradual decrease in P_{max} with higher AER is primarily attributed to the slower combustion rate and lower reactivity of ammonia. Replacing part of the DME with ammonia reduces the overall combustion rate, leading to delayed combustion and reduced peak pressure. The initial increase and subsequent decrease in HRR peak with rising AER can be explained by the enhanced combustion intensity in the low AER range, where DME promotes ammonia ignition. However, when the AER exceeds 60%, the limited DME content becomes insufficient to sustain strong flame propagation and ignition enhancement, leading to reduced combustion efficiency and a decline in the HRR peak. In addition, under the ADME-DF mode, the combustion phasing in the MCC is consistently delayed compared to that in the OCC across various AERs. This can be partially attributed to the shallower combustion chamber in MCC, which causes the DME spray to impinge on the wall prematurely, resulting in

kinetic energy loss and suboptimal initial fuel-air mixing. On the other hand, the removal of the squish region in MCC, though beneficial for promoting ammonia ignition, may also contribute to delayed combustion phasing.

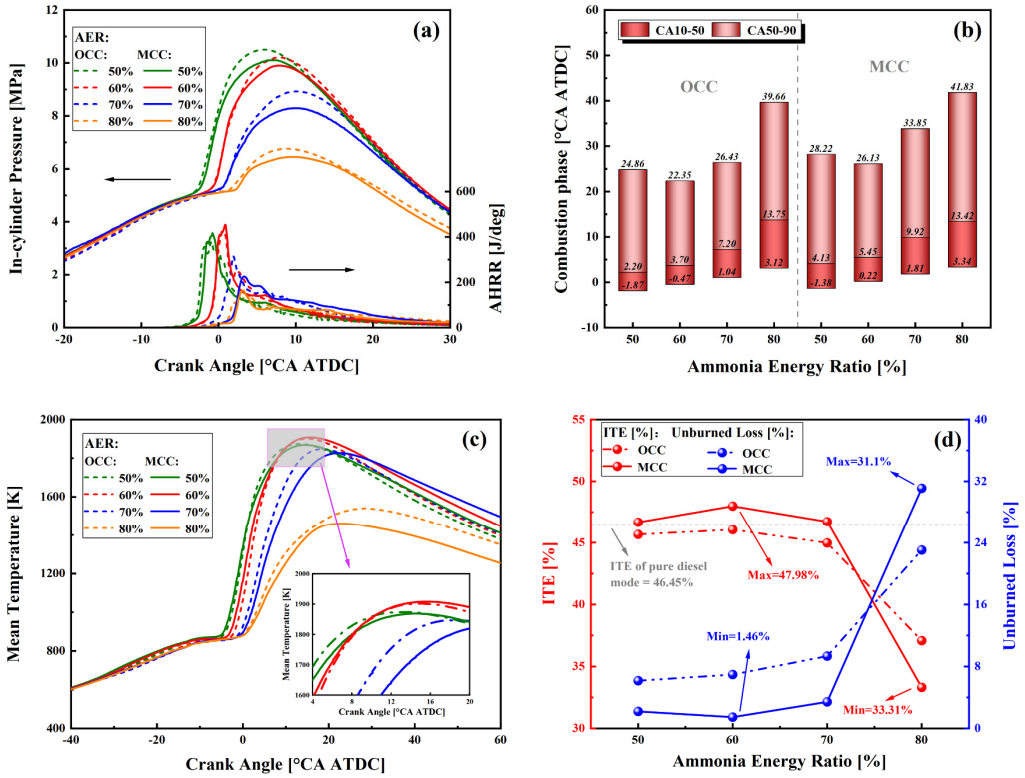


Figure 3. Effects of AER and CCG on combustion characteristics: (**a**) in-cylinder pressure and HRR; (**b**) combustion phasing; (**c**) mean temperature; (**d**) ITE and unburned losses.

Figure 3c,d illustrate the average in-cylinder temperature and indicated thermal efficiency (ITE) for OCC and MCC under various AERs. As AER increases, the overall combustion reactivity initially improves and then deteriorates, leading to the optimal heat release rate and concentration at an AER of 60%. Consequently, the peak in-cylinder temperature exhibits an initial rise followed by a decline. As shown in Figure 3d, the MCC configuration achieves higher ITE than OCC within the AER range of 50–70%, and also outperforms the conventional diesel mode. However, at an AER of 80%, MCC performs worse than OCC, with unburned energy losses reaching as high as 31.1%. This indicates that, without further parametric study, the advantages of MCC remain limited under high AER conditions.

Figure 4a,b compare the final emissions of unburned energy loss-related species between OCC and MCC under different AERs. It can be observed that with increasing AER, the emissions of uDME and uNH_3 increase, primarily due to the low reactivity of ammonia. At an AER of 60%, the uNH_3 emission from MCC is only 4.16 g/kW·h, representing an 85.46% reduction compared to OCC. However, at an AER of 80%, the uNH_3 emission of MCC reaches 148 g/kW·h, which is 38.3% higher than that of OCC. Since MCC eliminates the squish region present in OCC, it theoretically facilitates flame propagation and thus should reduce uDME and uNH_3 emissions. However, maintaining the OCC volume necessitates a reduction in chamber depth in MCC, causing DME spray to impinge on the wall earlier, resulting in kinetic energy loss and poor initial dual-fuel mixing, which ultimately leads to higher uNH_3 emissions at 80% AER compared to OCC. Similarly, at 80% AER, emissions of CO and unburned hydrocarbons (uHC), which contribute to minor

energy losses, are also higher in MCC than in OCC. The decrease in in-cylinder temperature is the main reason for the increased CO emissions, while the DME impingement on the wall delays combustion and causes incomplete droplet evaporation, resulting in increased uHC emissions.

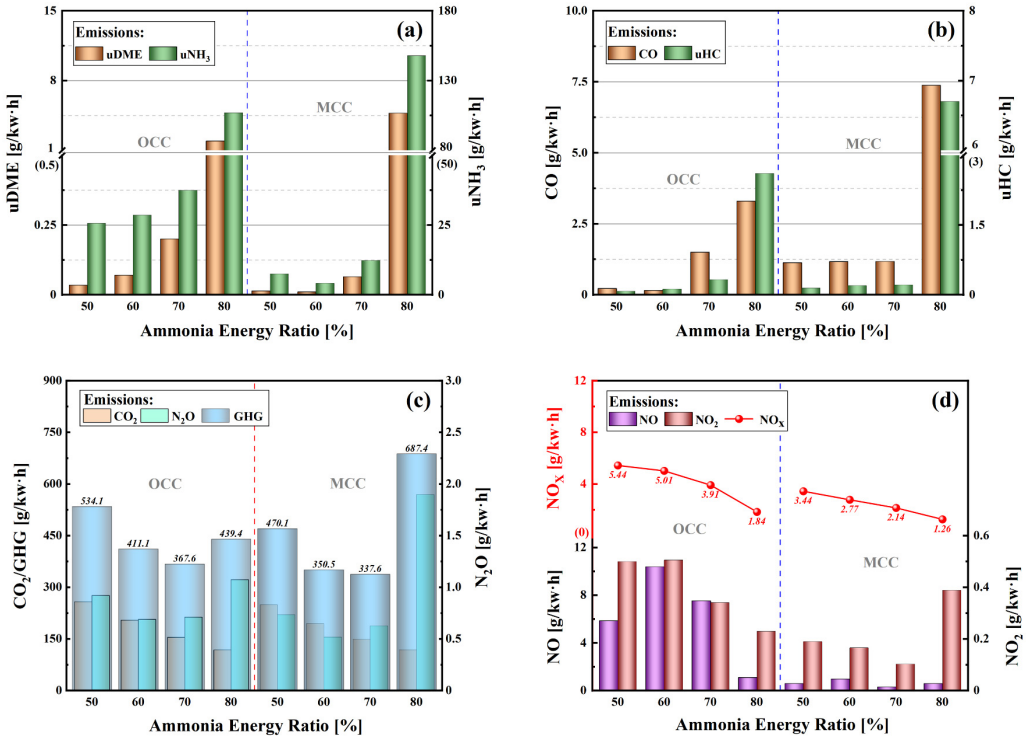


Figure 4. Effects of AER and CCG on emission characteristics: (**a**) uDME and uNH_3; (**b**) CO and uHC; (**c**) CO_2, GHG, and N_2O; (**d**) NO, NO_x, and NO_2.

As shown in Figure 4c, CO_2 emissions gradually decrease with the reduction in DME injection quantity. N_2O, which has a global warming potential up to 300 times greater than CO_2, is mainly formed in regions of moderate to low temperature, oxygen deficiency, and partial oxidation of ammonia. At an AER of 60%, MCC reduces GHG emissions by 14.8% compared to OCC. Due to the dominant magnitude of NO in total NO_x emissions, NO_x formation is primarily associated with NO. Unlike conventional diesel combustion, ammonia as a fuel contains nitrogen atoms, resulting in the formation of both thermal-NO_x and fuel- NO_x during the combustion process. Compared to OCC, the MCC design eliminates the squish region, allowing for more uniform flame propagation and reducing the occurrence of locally high-temperature, oxygen-rich zones. Consequently, NO_x emissions from MCC are consistently lower than those from OCC.

Changes in CCG can significantly affect in-cylinder flow and the formation of combustible mixtures. Therefore, it is necessary to adjust the injection strategy accordingly, such as the injection angle and timing, to optimize the spray development and mixture uniformity of DME, ensure reliable ignition, promote efficient synergistic combustion, and reduce emissions.

3.2. Effects of SIT and INA on the Performance of the ADME-DF Engine

This model is employed for full-cycle calculations of all three-dimensional CFD cases in this work, and fully accounts for convective and radiative heat transfer between the in-cylinder charge and the cylinder walls.

To fully exploit the potential of the MCC, this section investigates the effects of varying the single injection timing (SIT) and injection nozzle angle (INA) of DME at a constant

60% ammonia energy ratio (AER) to further improve combustion efficiency. Figure 5a,b compare in-cylinder pressure, HRR, and combustion phasing under different SITs and INAs in the single DME injection strategy. It is evident that advancing the DME injection timing raises the peak in-cylinder pressure and shortens the ignition delay time (IDT), which is attributed to improved fuel-air mixing. At an SIT of −15 °CA ATDC, increasing the INA results in higher peak pressure and HRR. However, when the SIT is advanced to −30 °CA ATDC, an INA of 85° results in a decrease in both pressure and HRR peaks. As shown in the inset of Figure 5a, at an INA of 85°, the DME spray tends to impinge on the cylinder wall, whereas at other angles, the spray mainly strikes the piston bowl. As shown in Figure 5b, in Case 1, increasing INA shortens the combustion duration. In contrast, in Strategy 2, an INA of 85° leads to an extended combustion duration.

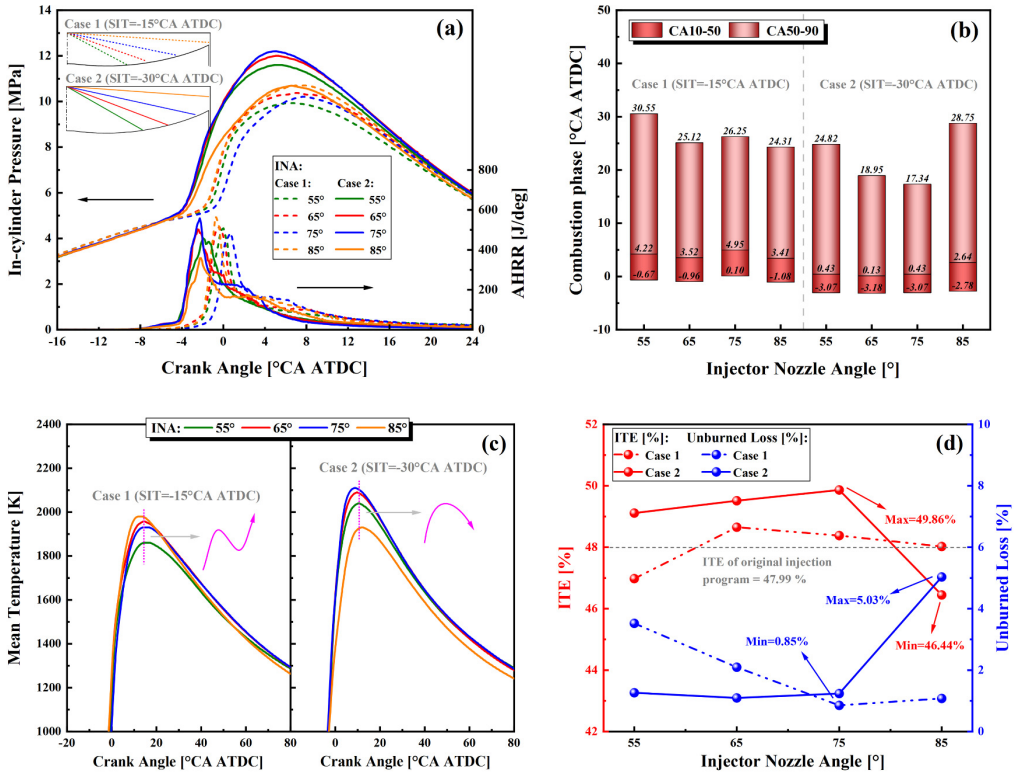


Figure 5. Effects of SIT and INA on combustion characteristics: (**a**) in-cylinder pressure and HRR; (**b**) combustion phasing; (**c**) mean temperature; (**d**) ITE and unburned losses.

As shown in Figure 5c, under varying SITs, the in-cylinder temperature peak first increases and then decreases with increasing INA. In Case 1, the peak temperature starts to decline when the INA reaches 75°. In Case 2, the temperature peak drops at an INA of 85°. This indicates that as the injection timing advances, the INA corresponding to the peak temperature decline shifts to a larger angle. As shown in Figure 5d, in Case 1, the maximum indicated thermal efficiency (ITE) of 48.65% occurs at an INA of 65°. In Case 2, the highest ITE of 49.86% is achieved at an INA of 75°, with an unburned energy loss of only 1.24%. This suggests that earlier injection timing is better matched with a larger INA.

To further analyze the effects of varying SITs and INAs on combustion and emissions, Figure 6a,b show longitudinal cross-sectional distributions of key parameters and species concentrations during the main combustion phase under different INAs for both cases. At an INA of 55°, the DME jet impinges on the piston bowl, travels along its edge, strikes the cylinder head, and finally disperses into the combustion chamber. At an INA of 85°, the DME spray is also influenced by the cylinder wall. When SIT is −15 °CA ATDC, the squish region formed by the piston and cylinder head enhances the rebound effect from

wall impingement, promoting more uniform in-cylinder fuel mixing. However, at the same INA of 85°, when the SIT is advanced to −30 °CA ATDC, some DME droplets form a stagnant film on the wall surface, reducing their contribution to effective mixing and reaction in the main combustion zone. This results in slower late-stage combustion and a longer combustion duration.

The SIT and INA of DME influence both in-cylinder combustion performance and emissions. In the ADME-DF engine, NO_x formation is a complex process. With a fixed AER of 60%, ammonia combustion efficiency directly affects fuel-NO formation, described by Equation (6), which primarily occurs at high combustion temperatures (T > 1400 K); Additionally, thermal-NO_x formation is influenced by in-cylinder temperature, the spatial and temporal distribution of high-temperature regions, and oxygen concentration. Specifically, NH_3 reacts with hydroxyl radicals (OH) and oxygen atoms to form NH_2 radicals, and NO is subsequently reduced within the temperature range of 1100–1400 K [50]. This reaction pathway is illustrated by Equations (7)–(10) [51]. The in-cylinder temperature and NO distributions in Figure 6a,b illustrate the formation characteristics.

$$NH_i + OX \rightarrow NO + NH_i \quad (8)$$

$$NH_3 + OH \rightarrow NH_2 + H_2O \quad (9)$$

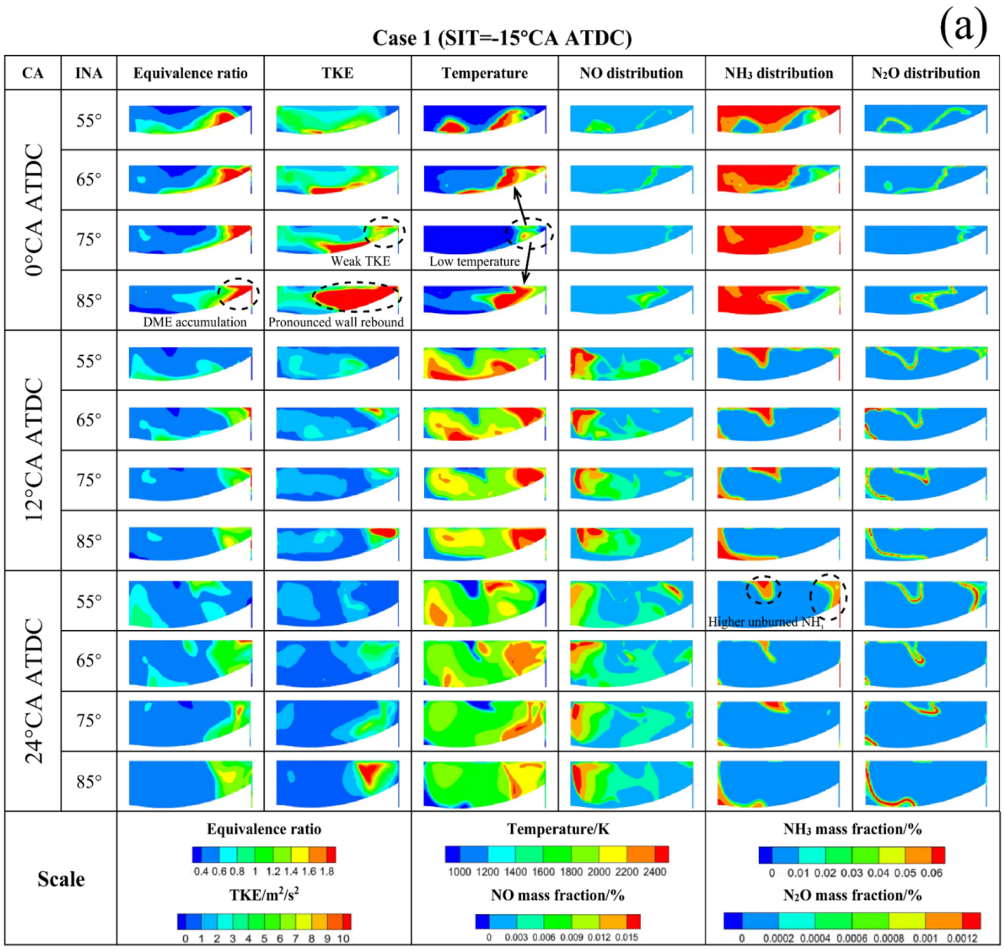


Figure 6. *Cont.*

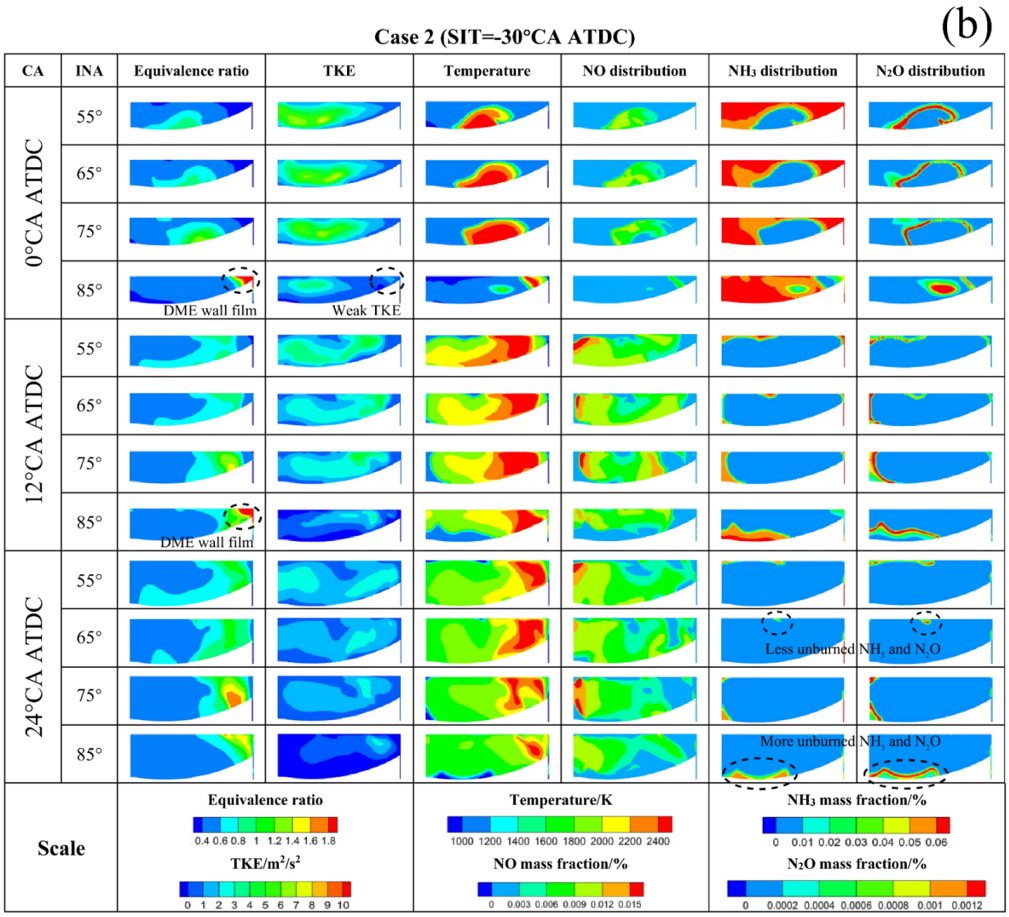


Figure 6. Effects of different INAs on the distribution of key parameters and species concentrations during the main combustion phase under different injection timings: (**a**) Case 1 (SIT = −15 °CA ATDC); (**b**) Case 2 (SIT = −30 °CA ATDC).

$$NH_3 + O \rightarrow NH_2 + OH \quad (10)$$

$$NH_2 + NO \rightarrow N_2 + H + OH \quad (11)$$

$$NH_2 + NO \rightarrow N_2 + H_2O \quad (12)$$

As shown in Figure 6a,b, in Case 1, uNH_3 concentration is higher at an INA of 55° compared to other INAs, primarily distributed near the cylinder wall and cylinder head away from the center of the piston bowl. In Case 2, uNH_3 is highest at an INA of 85°, with concentrations primarily located at the center of the piston bowl. This indicates that a proper combination of injection nozzle angle and timing can improve in-cylinder dual-fuel mixing, mitigate overly rich or lean regions. Furthermore, N_2O, a product of incomplete ammonia combustion, primarily forms at the leading edge of the NH_3 flame. Its formation pathway, described by Equations (10) and (11), primarily occurs at temperatures below 1400 K [52]. However, the figure does not clearly present a quantitative comparison of final emissions, such as NO and N_2O, under different injection strategies.

$$NH + NO \rightarrow N_2O + H \quad (13)$$

$$NH_2 + NO_2 \rightarrow N_2O + H \quad (14)$$

As shown in Figure 7a,b, advancing the injection timing lowers the in-cylinder temperature, promoting DME condensation on the piston and cylinder walls and forming a

liquid film that hinders combustion, thereby increasing uDME emissions [53]. Furthermore, in Case 1, an INA of 85° enhances DME ignition and ammonia reactivity, resulting in uNH_3 emission of only 1.55 g/kW·h, a reduction of 62.74% compared to the original MCC injection strategy. Similarly, in Case 1, an INA of 65° results in CO and uHC emissions of 0.2 g/kW·h and 0.02 g/kW·h, respectively, representing reductions of 82.9% and 90.1% compared to the original strategy. As illustrated in Figure 7c,d, the minimum GHG and NO_x emissions occur at an INA of 65° in Case 2 and 75° in Case 1, respectively, corresponding to reductions of 54.8% and 86.1% compared to the conventional diesel mode. These minimum GHG and NO_x values are primarily influenced by in-cylinder temperature, spray targeting, and mixture formation, underscoring the capability of injection strategies for precise multi-pollutant control.

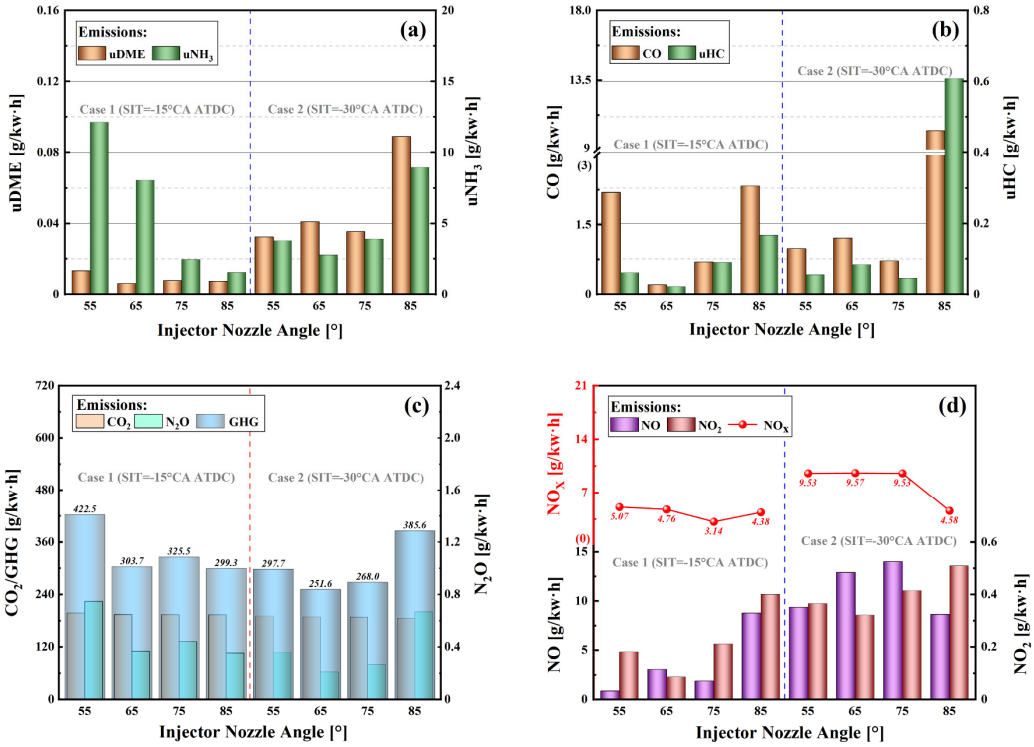


Figure 7. Effects of SIT and INA on emission characteristics: (**a**) uDME and uNH_3; (**b**) CO and uHC; (**c**) CO_2, GHG, and N_2O; (**d**) NO, NO_x, and NO_2.

To comprehensively reveal the coupled effects of SIT and INA on combustion and emission characteristics of the ADME-DF engine, Figure 8a,b present contour plots of uNH_3 emissions and ITE under various DME injection timings and angles. Under an AER of 60%, elevated uNH_3 emissions are concentrated in the central, upper-left, and lower-right regions of the figures. Specifically, with relatively advanced injection timings, larger INAs help reduce uNH_3 emissions, whereas smaller angles are better suited to delayed injection timings. Additionally, when SIT is set to −10 °CA ATDC, the engine exhibits suboptimal combustion performance, with ITE remaining at a low level. This is primarily attributed to the insufficient mixing of NH_3 and DME, which prolongs the combustion duration and reduces combustion efficiency.

Figure 8c,d illustrate the distributions of GHG and NO_x emissions. In Figure 8c, the variation in GHG emissions is primarily attributed to N_2O, and a comparison with Figure 8a reveals similar spatial patterns. From a macroscopic perspective, N_2O is a byproduct of incomplete NH_3 combustion; therefore, elevated uNH_3 emissions indicate inefficient NH_3 oxidation, leading to increased N_2O formation and degraded combustion performance.

On a microscopic level, oxygen-deficient regions, combined with underdeveloped radical chain reactions, inhibit the complete conversion of NH_3 to N_2, favoring the formation of N_2O as an intermediate product. Thus, increased uNH_3 emissions not only reflect incomplete combustion but also signify low radical concentrations (e.g., O, H, OH), insufficient reaction chain propagation, and interrupted oxidation pathways, all of which promote N_2O accumulation.

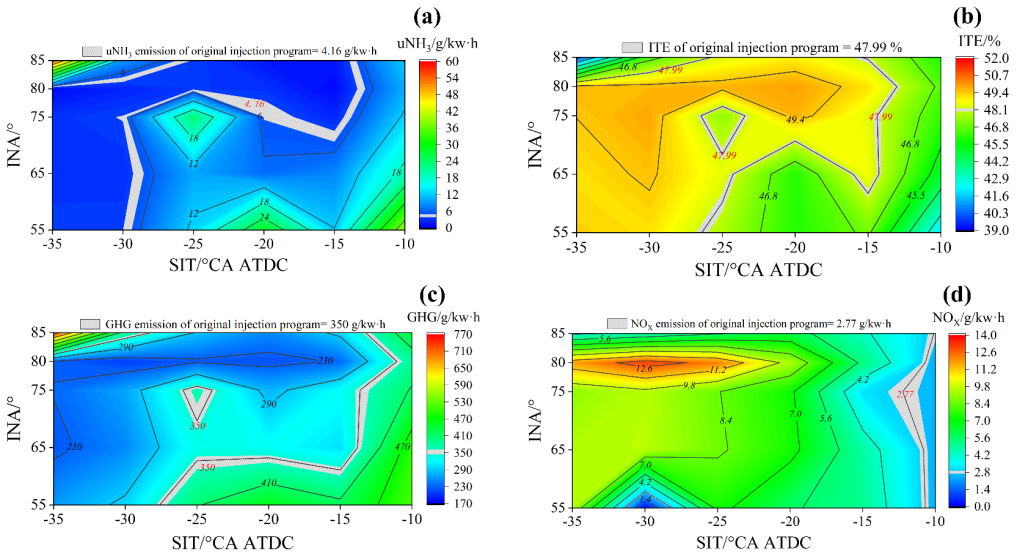


Figure 8. Effects of different SITs and INAs on the performance of the ADME-DF engine: (**a**) uNH_3 emissions; (**b**) ITE; (**c**) GHG emissions; (**d**) NO_x emissions.

In Figure 8d, within the range of relatively advanced SITs, NO_x emissions increase with earlier injection, while the influence of INA is comparatively limited. However, when the SIT is advanced to −30 °CA ATDC, INA has a pronounced effect on NO_x emissions. Given that the AER is fixed at 60%, NO_x emissions are primarily governed by the formation of thermal-NO_x. Typically, advancing the injection timing leads to more uniform fuel mixing, shortens both ignition delay time (IDT) and combustion duration (CD), and leads to a rapid increase in in-cylinder temperature, collectively contributing to elevated NO_x emissions. Moreover, the combined variation in injection timing and angle alters the spray characteristics DME, which also changes the wall-impingement timing and subsequently affects fuel mixing.

It is worth noting that in the practical application of ADME-DF engines, attention should not only be paid to combustion and emission characteristics, but also to the avoidance of abrupt in-cylinder pressure rise in order to reduce the risk of engine knock and ensure operational stability. As shown in Figure 9a,b, it is difficult to meet the MPRR limitation and RI requirements solely by adjusting the injection nozzle angle or injection timing. MPRR typically occurs near CA10, and while the single injection strategy enhances engine performance by improving fuel mixing, it also concentrates the combustion of a large amount of fuel, causing a rapid rise in in-cylinder pressure and excitation of the natural frequency oscillations of the cylinder block and combustion chamber structure. Therefore, the next section will investigate the effects of a split injection strategy on ADME-DF engine performance, with the aim of ensuring engine reliability and durability.

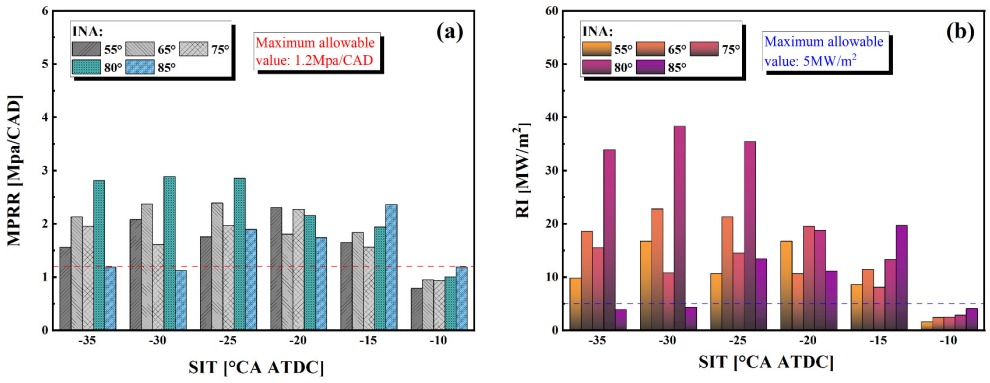


Figure 9. Effects of different SITs and INAs on the operating stability of the ADME-DF engine: (**a**) MPRR; (**b**) RI.

3.3. Effects of Split Injection Strategy on the Performance of the ADME-DF Engine

The split injection strategy can optimizes the heat release process and controls the combustion rate by adjusting the pilot injection ratio (PIR), pilot injection timing (PIT), and main injection timing (MIT), thereby enhancing high thermal efficiency and reducing emissions while satisfying the maximum pressure rise rate (MPRR) constraints. To balance combustion efficiency and NO_x emissions, this section investigates the effects of split injection strategies on the ADME-DF engine by varying the PIR and PIT, while keeping the MIT fixed at −5 °CA ATDC.

As shown in Figure 10a,b, the peak in-cylinder pressure increases with the pilot injection ratio (PIR) under varying PITs. Moreover, as the PIT is further advanced, the dual-peak characteristic of the HRR becomes more pronounced. This is because at a PIT of −60 °CA ATDC, DME has ample time for evaporation and mixing, leading to the formation of a flammable mixture that ignites prior to the main injection, causing early heat release. This results in a more evident dual-peak in the heat release rate, and as the pilot injection amount increases, the premixed combustion is enhanced, elevating the first heat release peak to rise. Combustion phasing generally advances with earlier PIT and increased PIR. Ignition sources or high-reactivity zones formed by pilot injection facilitate the combustion of the main injection. However, at a PIT of −60 °CA ATDC, the reactive zones may be depleted or quenched before the main injection, leading to a net delay in combustion. Consequently, the combustion phasing is delayed. Furthermore, at a PIT of −40 °CA ATDC with an excessively high PIR (e.g., 80%), the early-injected DME forms an overly rich or unevenly distributed mixture, which reduces reactivity and delays the onset of ignition. This leads to an anomalous delay in the CA10.

As shown in Figure 10c, compared with Case 3, advancing the PIT in Case 4 results in a decrease in the average in-cylinder temperature. This is because at −60 °CA ATDC, both the in-cylinder pressure and temperature are comparatively low. The injected fuel has not yet participated in heat release reactions, and the atomized DME exhibits limited evaporation capability. A portion condenses on the cylinder walls or piston crown, reducing both local and overall temperatures. As PIR increases, more fuel is involved in low-temperature oxidation and localized auto-ignition during the compression stroke, thereby raising the average end-of-compression temperature. As shown in Figure 10d, Case 3 exhibits higher ITE compared to Case 4. At PIR = 80%, ITE reaches a peak value of 49.51%. This represents a 1.52% increase compared to the original injection strategy. Meanwhile, unburned energy losses are minimized to just 0.91%.

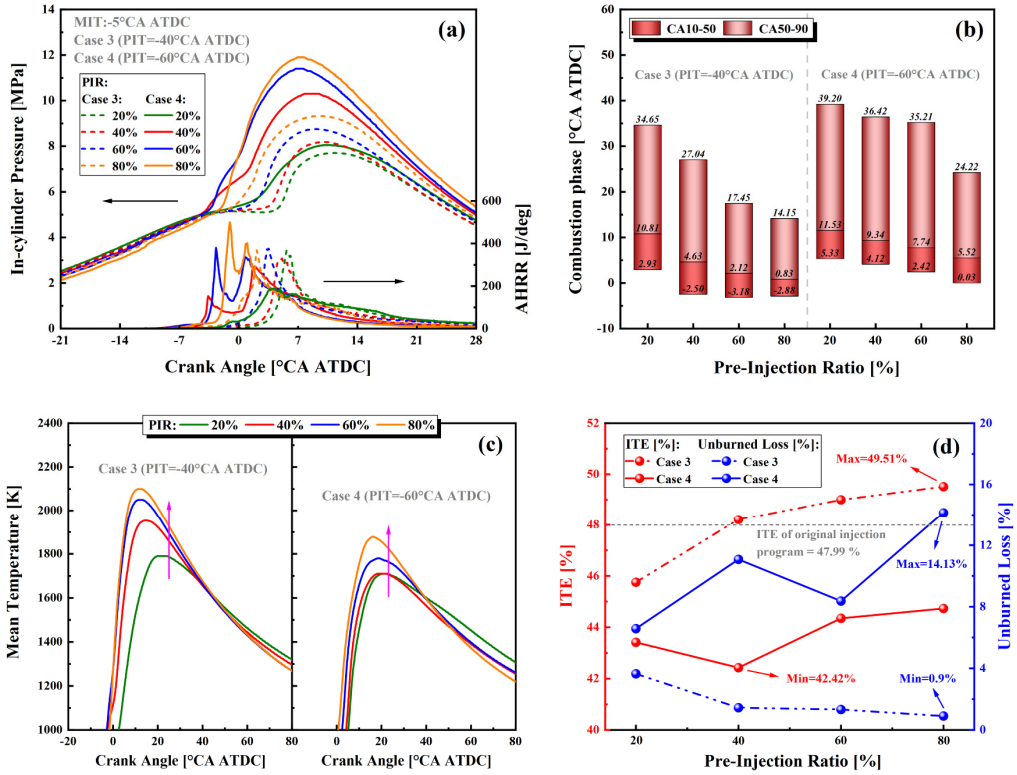


Figure 10. Effects of PIT and PIR on combustion characteristics: (**a**) In-cylinder pressure and HRR; (**b**) Combustion phasing; (**c**) mean temperature; (**d**) ITE and unburned loss.

By comparing Figure 11a,b, it can be observed that the uDME emissions in Case 4 are significantly higher than those in Case 3, especially when PIR $\geq$ 40%. This is primarily attributed to lower in-cylinder temperature and pressure, which facilitate DME condensation on cylinder walls after injection, hindering full fuel participation in combustion. As a result, uNH_3 emissions also remain elevated in Case 4. Furthermore, CO and uHC emissions are higher in Case 4 than in Case 3, mainly due to low-temperature combustion and excessive mixture dilution. According to Figure 11c, CO_2 emissions slightly decline as PIR increases. This occurs because an increase in PIR corresponds to a decrease in MIR, in the main injection phase, higher fuel concentration and elevated temperatures promote more complete DME combustion. However, pre-injected DME may evaporate prematurely, diffuse excessively, or form liquid films on cold surfaces during compression, reducing combustion efficiency. As the contribution from main injection combustion diminishes, the effective conversion of DME to CO_2 decreases, thereby reducing overall CO_2 emissions.

Furthermore, N_2O emissions in Case 4 are considerably higher than those in Case 3. This is primarily due to the earlier pre-injection leading to lower in-cylinder temperatures, inadequate fuel evaporation and mixing, and non-uniform fuel–air distribution during the compression process. These conditions suppress the instantaneous heat release following the main injection and reduce the overall combustion temperature, thereby favoring N_2O formation over NO_x. In Case 3, at a PIR of 80%, GHG emissions reach a minimum of 284 g/kW·h, indicating an 18.86% reduction relative to the original injection strategy. As shown in Figure 11d, although NO_x emissions in Case 4 are lower than in Case 3, the ITE in Case 4 is lower, as indicated in Figure 10d. In Case 3, at a PIR of 80%, the maximum ITE reaches 49.51%, with corresponding NO_x emissions of 9.4 g/kW·h. Although this value is slightly higher than that under the MCC original injection strategy, it is 58.22% lower than that in the pure diesel mode.

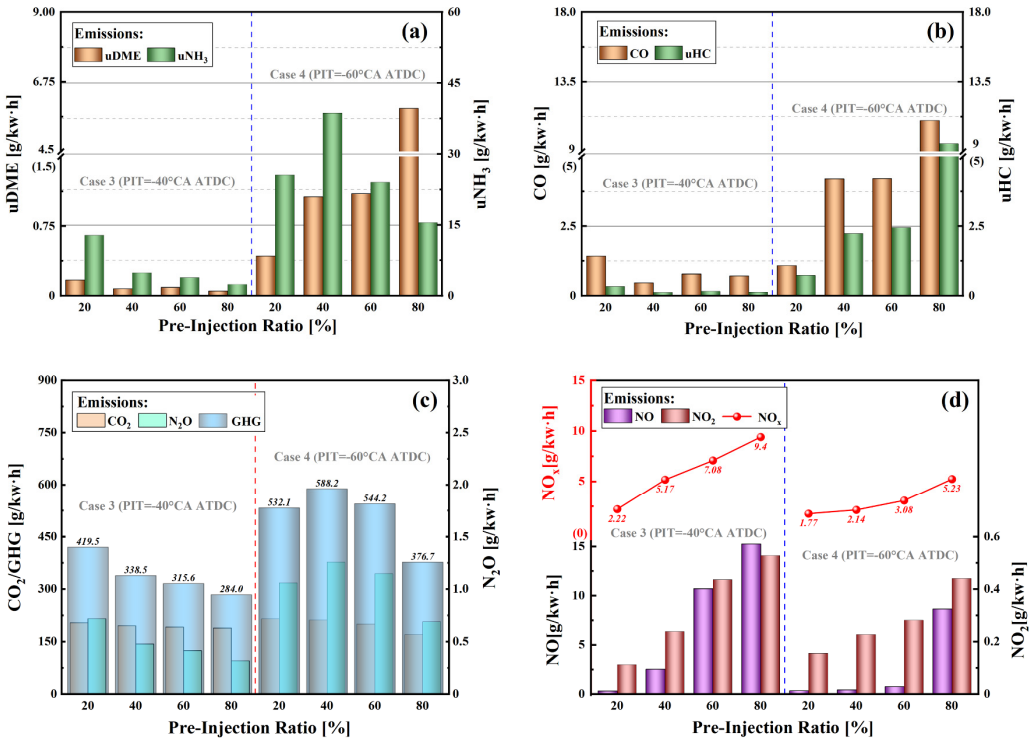


Figure 11. Effects of PIT and PIR on emission characteristics: (**a**) uDME and uNH_3; (**b**) CO and uHC; (**c**) CO_2, GHG, and N_2O; (**d**) NO, NO_x, and NO_2.

To comprehensively evaluate the impact of split injection strategies on the performance of ADME-DF engines, it is necessary to broaden the parameter range of PIT and PIR, in order to systematically investigate the coupling effects of pilot injection timing and quantity distribution on thermal efficiency and emissions. As shown in Figure 12a,b, with MIT fixed at −5 °CA ATDC, regions with lower uNH_3 emissions and higher ITE are observed in the upper right corner. However, when PIT is excessively advanced, part of the DME may prematurely autoignite or form a liquid film on the wall surface, impairing the mixing uniformity of the dual fuels, leading to increased uNH_3 emissions and reduced ITE. In Figure 12c,d, the GHG and NO_x emissions exhibit inverse trends. In ADME-DF engines, since the AER is fixed at 60%, the variation in GHG emissions is mainly driven by N_2O, whose global warming potential is up to 300 times greater than CO_2. Conversely, NO_x emissions can be approximated by NO concentrations, which mainly form in high-temperature zones, while N_2O tends to form in low-temperature, ammonia-rich, or oxygen-deficient regions. As a result, these two species exhibit distinctly opposing trends under varying combustion conditions. As seen in Figure 12b, higher ITE is often accompanied by elevated NO_x emissions, which can be effectively mitigated using aftertreatment technologies.

As can be observed from Figure 13a,b in conjunction with Figure 9, the split injection strategy extends the heat release process and reduces combustion concentration by controlling fuel distribution and combustion phasing. Compared with the single injection strategy, it achieves a significant reduction in both MPRR and RI, which lowers knock propensity, improves combustion stability, and mitigates overall knock risk.

In summary, adjusting the SIT and INA of DME can further improve the combustion efficiency and reduce emissions of the ADME-DF engine, building on the newly designed combustion chamber. However, excessively advanced SIT or an inappropriate INA may intensify premixed combustion or lead to non-uniform fuel-air mixing, causing significant in-cylinder pressure oscillations and increasing the risk of knocking.

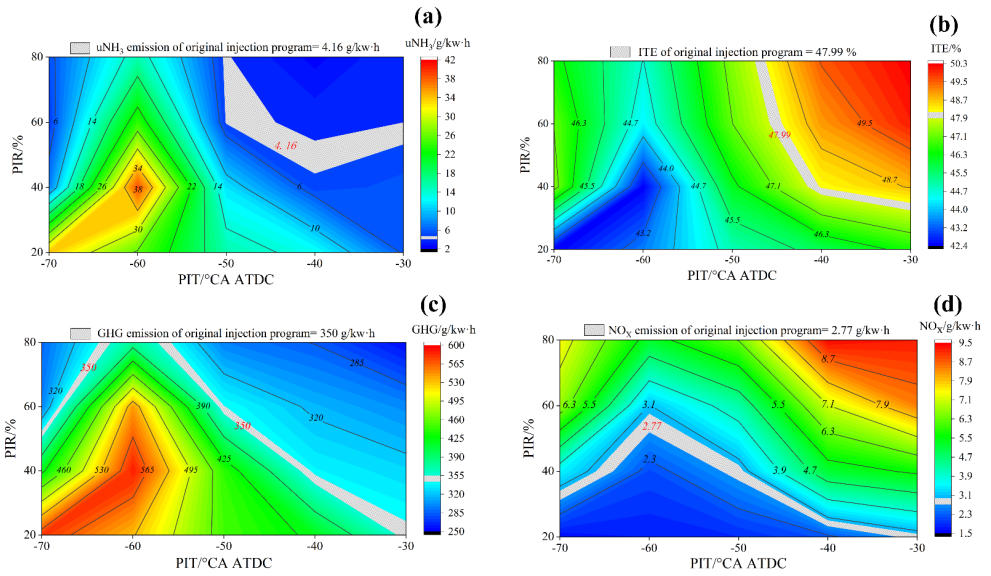


Figure 12. Effects of different PITs and PIRs on the performance of the ADME-DF engine: (**a**) uNH_3 emissions; (**b**) ITE; (**c**) GHG emissions; (**d**) NO_x emissions.

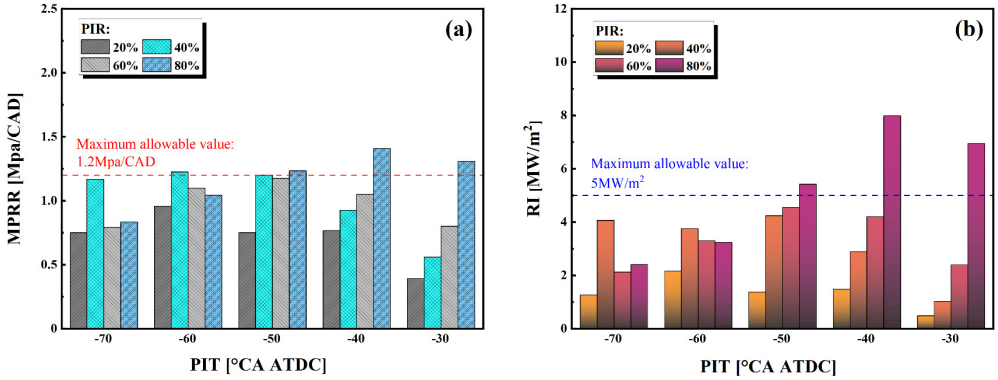


Figure 13. Effects of different PITs and PIRs on the operating stability of the ADME-DF engine: (**a**) MPRR; (**b**) RI.

Figure 14 provides a comprehensive comparison of the effects of different injection strategies on combustion and emission characteristics under the condition of maximum ITE. As shown in Figure 14a, under the single injection strategy, the highest ITE occurs at an INA of 75°, but this is accompanied by relatively high pollutant emissions. Reducing emissions requires a compromise in ITE, since both SIT and INA jointly affect the uniformity of the fuel-air mixture. Comparison of Figure 14a,b reveals that the split injection strategy, through the introduction of pilot injection to guide combustion, moderates the heat release rate, reduces the MPRR, and enhances combustion stability. Moreover, with MIT fixed at −5 °CA ATDC, the corresponding PITs for maximum ITE are all at −30 °CA ATDC under different PIRs, indicating good consistency in combustion and emission performance, along with improved operational stability.

The core performance indicators of the optimal scheme are summarized in Table 7. With the proposed split injection strategy, the engine achieves the highest indicated thermal efficiency, realizes remarkable GHG and NO_x abatement relative to the pure diesel mode, and ensures reliable operation by mitigating in-cylinder pressure oscillations.

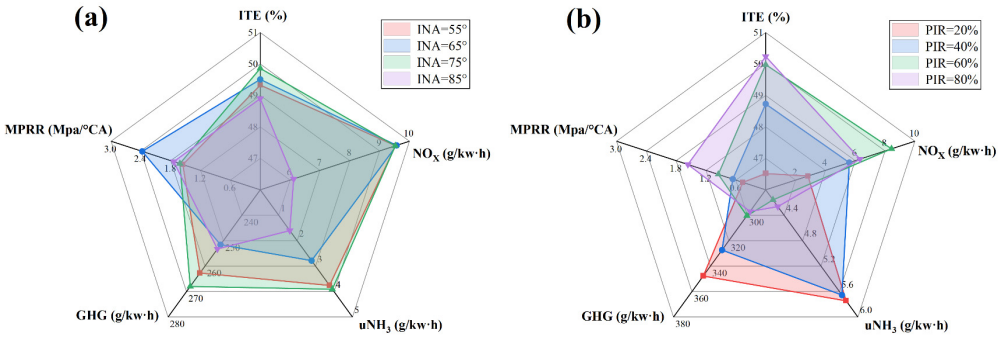


Figure 14. Comprehensive comparison of combustion and emission characteristics under different injection strategies: (**a**) Single injection; (**b**) Split injection.

Table 7. Core performance of the optimal operating condition.

Item	Optimal Condition Result
Injection strategy	Split injection: MIT = −5 °CA ATDC, PIT = −30 °CA ATDC, PIR = 60%
Indicated thermal efficiency (ITE)	49.98%, outperforming single-injection strategy and pure diesel mode
Unburned ammonia (uNH_3)	4.16 g/kW·h, maintained at a low emission level
Greenhouse gas (GHG)	45.94% reduction compared with pure diesel mode
Nitrogen oxides (NO_x)	62.49% reduction compared with pure diesel mode
Operational stability	Satisfies knock constraints, with significantly suppressed in-cylinder pressure oscillation

4. Conclusions

In this study, a three-dimensional simulation model of an ADME-DF engine was developed, and the combustion chamber geometry was optimized according to the dual-fuel combustion characteristics to reduce unburned NH_3 emissions. Furthermore, using the optimized combustion chamber and an ammonia energy ratio (AER) of 60%, the effects of various DEM injection strategies on combustion and emissions performance were investigated. The main conclusions are as follows:

(1) Optimizing the combustion chamber geometry by removing the original squish area effectively expanded the flame propagation zone, improved combustion efficiency, and reduced pollutant emissions. Under ADME-DF conditions with AER = 60%, the new combustion chamber raised ITE by 1.93%, reduced GHG emissions by 14.8%, cut uNH_3 emissions by 85.46%, and decreased NO_x emissions by 44.7%, compared with the original chamber design. Optimizing the single injection timing and injection nozzle angle of DME significantly improved the mixing uniformity of the dual-fuel–air mixture, further enhancing combustion efficiency. At relatively advanced injection timings, a larger INA led to lower uNH_3 emissions, while a smaller angle was better matched with more delayed injection timings. In the ADME-DF mode with AER = 60%, the new combustion chamber achieved a peak ITE of 49.87% when using a single injection timing of −30 °CA ATDC and an INA of 75°, with GHG emissions reduced by 23.42% compared to the original strategy. However, the corresponding MPRR and RI exceeded acceptable limits, increasing the risk of knock.

(2) Compared to the single injection strategy, the split injection strategy reduces combustion concentration, ensuring stable engine operation while achieving high thermal efficiency and low emissions. At an MIT of −5 °CA ATDC, PIT of −30 °CA ATDC, and PIR of 60%, the ITE reached 49.98%, representing a 1.99% increase compared to the original injection strategy. GHG emissions were reduced by 14.29%, and NO_x

emissions slightly increased, yet remained 62.49% lower than in the pure diesel mode. The uNH_3 emissions were only 4.16 g/kW·h.

(3) The variation trend of ITE was generally inversely related to that of GHG emissions (primarily N_2O-driven), and similar to that of NO_x (NO + NO_2) emissions. This is because in ADME-DF engines, improved combustion efficiency leads to higher ITE and suppresses the formation of incomplete combustion products such as N_2O. However, the resulting increase in in-cylinder temperature promotes NO_x formation. Therefore, ITE is positively correlated with NO_x and negatively correlated with GHG emissions. In practical applications, technologies like exhaust gas recirculation (EGR) and selective catalytic reduction (SCR) can be employed to effectively mitigate total NO_x emissions. Building on the findings from the specific operating conditions examined in this work, future investigations will seek to advance the engineering application of ammonia/dimethyl ether (NH_3/DME) dual-fuel engines. Optical diagnostic experiments will be performed to acquire microscale combustion data with high temporal and spatial resolution, supporting further calibration and refinement of the three-dimensional CFD model.

(4) In addition, the study will be extended to full speed and load operating maps, and adaptive injection strategies will be developed to address ignition challenges at low loads as well as the sharp rise in knock propensity and NO_x emissions at high loads. The limiting constraints imposed by burning rate and reactivity limits at higher ammonia energy ratios (AER > 60%) will also be explored in depth. Combined with system-level coordinated control integrating in-cylinder split injection, EGR and SCR aftertreatment, this research aims to achieve a comprehensive trade-off between high combustion efficiency and ultra-low pollutant and greenhouse gas emissions.

(5) For practical engineering development of ammonia–dimethyl ether dual-fuel engines with port-fuel-injected ammonia and direct-injected DME, two targeted design recommendations are summarized based on the simulation results. First, an open-type combustion chamber without the squish region, matched with an appropriately enlarged injector nozzle angle, is recommended to enhance flame propagation and suppress unburned ammonia slip. Second, the split DME injection strategy with a pilot injection ratio of approximately 60% at −30 °CA ATDC and main injection at −5 °CA ATDC is preferred for application. Compared with the single-injection scheme, it achieves comparable high thermal efficiency while significantly reducing the maximum pressure rise rate and ringing intensity, thus improving the operational reliability of the engine. For practical engineering development of ammonia–dimethyl ether dual-fuel engines with port-fuel-injected ammonia and direct-injected DME, two targeted design recommendations are summarized based on the simulation results. First, an open-type combustion chamber without the squish region, matched with an appropriately enlarged injector nozzle angle, is recommended to enhance flame propagation and suppress unburned ammonia slip. Second, the split DME injection strategy with a pilot injection ratio of approximately 60% at −30 °CA ATDC and main injection at −5 °CA ATDC is preferred for application. Compared with the single-injection scheme, it achieves comparable high thermal efficiency while significantly reducing the maximum pressure rise rate and ringing intensity, thus improving the operational reliability of the engine.

Author Contributions: Conceptualization, Y.W. and X.M.; methodology, Y.W.; software, Y.W.; validation, Y.W., Z.Y. and J.Z.; formal analysis, X.M.; investigation, Y.W.; resources, Y.W.; data curation, Y.W., X.M. and Y.D.; writing—original draft preparation, Y.W.; writing—review and editing, X.M., Y.D. and J.Z.; visualization, Y.W.; supervision, X.M., Y.D. and J.Z.; project administration, X.M. All authors have read and agreed to the published version of the manuscript.

Funding: This research received no external funding, The APC was funded by Yize Wang.

Data Availability Statement: The data used in this study are available from the corresponding author upon reasonable request.

Conflicts of Interest: The authors declare no conflicts of interest.

Abbreviations

The following abbreviations are used in this manuscript:

AER	Ammonia Energy Ratio
ATDC	After Top Dead Center
HRR	Heat Release Rate
LPDF	Low-Pressure injection Dual Fuel
CI	Compression-Ignition
SOI	Start Of Injection
ITE	Indicated Thermal Efficiency
IVC	Intake Valve Closing
EVC	Exhaust Valve Closing
GHG	Greenhouse gas
SAGE	Scalar Edged Flamelet Model
CCG	Combustion chamber geometry
MCC	Modified combustion chamber
INA	DME injection nozzle angle
PIT	DME pre-injection timing
MPRR	Maximum cylinder pressure rise rate
GWP	Global Warming Potential
ADME-DF	Ammonia–Dimethyl Ether Dual-Fuel
CA	Crank Angle
CFD	Computational Fluid Dynamics
HPDF	High-Pressure injection Dual Fuel
LHV	Lower Heating Value
EOI	End Of Injection
IMEP	Indicated Mean Effective Pressure
IVO	Intake Valve Opening
EVO	Exhaust Valve Opening
NO_x	Nitrogen Oxides
RNGk-ε	Re-Normalization Group k-Epsilon
NTC	Non-Constant Temperature Coefficient
OCC	Original combustion chamber
SIT	DME single injection timing
MIT	DME main injection timing
PIR	DME pre-injection ratio
RI	Ringing intensity

References

1. Dhanapal, B.; Venkatesan, H.; Moorthy, B. Synergetic effect of hydrogen supplementation with waste cooking oil biodiesel—An assessment of the emission, combustion and performance parameters of a compression ignition engine. *Int. J. Hydrogen Energy* **2024**, *49*, 1292–1302. [CrossRef]
2. Teoh, Y.H.; How, H.G.; Le, T.D.; Nguyen, H.T.; Loo, D.L.; Rashid, T.; Sher, F. A review on production and implementation of hydrogen as a green fuel in internal combustion engines. *Fuel* **2023**, *333*, 126525. [CrossRef]
3. Kurien, C.; Mittal, M. Review on the production and utilization of green ammonia as an alternate fuel in dual-fuel compression ignition engines. *Energy Convers. Manag.* **2022**, *251*, 114990. [CrossRef]

4. Wen, L.; Zhu, Q.; Zeng, J.; Deng, H.; Chen, G.; Wen, X.; Wang, F.; Hao, Q. The effects of NH3 pre-cracking and initial temperature on the intrinsic instability and NOx emissions of NH3/bio-syngas/air premixed flames. *J. Energy Inst.* **2024**, *117*, 101873. [CrossRef]
5. Shrestha, K.P.; Eckart, S.; Elbaz, A.M.; Giri, B.R.; Fritsche, C.; Seidel, L.; Roberts, W.L.; Krause, H.; Mauss, F. A comprehensive kinetic model for dimethyl ether and dimethoxymethane oxidation and NOx interaction utilizing experimental laminar flame speed measurements at elevated pressure and temperature. *Combust. Flame* **2020**, *218*, 57–74. [CrossRef]
6. Okafor, E.C.; Naito, Y.; Colson, S.; Ichikawa, A.; Kudo, T.; Hayakawa, A.; Kobayashi, H. Measurement and modelling of the laminar burning velocity of methane-ammonia-air flames at high pressures using a reduced reaction mechanism. *Combust. Flame* **2019**, *204*, 162–175. [CrossRef]
7. Schirru, A.; Lucchini, T.; D'Errico, G.; Mehl, M.; Hilfiker, T.; Soltic, P. Numerical investigation on the use of Dimethyl Ether (DME) as an alternative fuel for compression-ignition engines. *Fuel* **2023**, *354*, 129434. [CrossRef]
8. Zhu, J.; Zhou, D.; Yang, W.; Qian, Y.; Mao, Y.; Lu, X. Investigation on the potential of using carbon-free ammonia in large two-stroke marine engines by dual-fuel combustion strategy. *Energy* **2023**, *263*, 125748. [CrossRef]
9. Yousefi, A.; Guo, H.; Dev, S.; Liko, B.; Lafrance, S. Effects of ammonia energy fraction and diesel injection timing on combustion and emissions of an ammonia/diesel dual-fuel engine. *Fuel* **2022**, *314*, 122723. [CrossRef]
10. Huang, Z.; Zhang, W.G.; Han, D.; Zhu, L.; Lin, H.; Guan, B. Dimethyl ether: A promising fuel for marine engines. *Front. Energy* **2025**, *19*, 28. [CrossRef]
11. Good, D.A.; Francisco, J.S.; Jain, A.K.; Wuebbles, D.J. Lifetimes and global warming potentials for dimethyl ether and for fluorinated ethers: CH_3OCF_3 (E143a), CHF_2OCHF_2 (E134), CHF_2OCF_3 (E125). *J. Geophys. Res. Atmos.* **1998**, *103*, 28181–28186. [CrossRef]
12. Arcoumanis, C.; Bae, C.; Crookes, R.; Kinoshita, E. The potential of di-methyl ether (DME) as an alternative fuel for compression-ignition engines: A review. *Fuel* **2008**, *87*, 1014–1030. [CrossRef]
13. Gross, C.W.; Kong, S.-C. Performance characteristics of a compression-ignition engine using direct-injection ammonia–DME mixtures. *Fuel* **2013**, *103*, 1069–1079. [CrossRef]
14. Ryu, K.; Zacharakis-Jutz, G.E.; Kong, S.-C. Performance characteristics of compression-ignition engine using high concentration of ammonia mixed with dimethyl ether. *Appl. Energy* **2014**, *113*, 488–499. [CrossRef]
15. Li, B.; Wang, Q.; Dai, L.; He, Z. Numerical study on combustion and emission characteristics of a dual-fuel direct injection marine engine using ammonia/DME mixtures. *Appl. Therm. Eng.* **2025**, *263*, 125383. [CrossRef]
16. Shi, X.; Xiong, Q.; Wang, H.; Han, K.; Liu, L.; Pan, C.; Zhao, J. Innovative method of in-cylinder purification emission control in low-speed marine engines: Numerical study on ammonia/diesel high-pressure direct injection. *Appl. Therm. Eng.* **2025**, *267*, 125769. [CrossRef]
17. Giddey, S.; Badwal, S.P.S.; Kulkarni, A. Review of electrochemical ammonia production technologies and materials. *Int. J. Hydrogen Energy* **2013**, *38*, 14576–14594. [CrossRef]
18. Doppalapudi, A.T.; Azad, A.K.; Khan, M.M.K.; Than Oo, A.M. Effect of different chamber geometries on combustion formation to reduce harmful emissions. *Appl. Therm. Eng.* **2025**, *261*, 125073. [CrossRef]
19. Wang, X.; Li, T.; Zhou, X.; Huang, S.; Chen, R.; Yi, P.; Lv, Y.; Wang, Y.; Rao, H.; Liu, Y.; et al. Reductions in GHG and unburned ammonia of the pilot diesel-ignited ammonia engines by diesel injection strategies. *Appl. Therm. Eng.* **2025**, *260*, 124967. [CrossRef]
20. Gültekin, N.; Ciniviz, M. Examination of the effect of combustion chamber geometry and mixing ratio on engine performance and emissions in a hydrogen-diesel dual-fuel compression-ignition engine. *Int. J. Hydrogen Energy* **2023**, *48*, 2801–2820. [CrossRef]
21. Shin, J.; Park, S. Numerical analysis for optimizing combustion strategy in an ammonia-diesel dual-fuel engine. *Energy Convers. Manag.* **2023**, *284*, 116980. [CrossRef]
22. Liu, J.; Wang, J.; Zhao, H. Optimization of the injection parameters and combustion chamber geometries of a diesel/natural gas RCCI engine. *Energy* **2018**, *164*, 837–852. [CrossRef]
23. Ye, L.; Zhou, R.; Chen, W.; Gong, S.; Zhou, X.; Li, J. Effect of in-cylinder flow on the combustion and flame propagation characteristics of an ammonia/diesel dual-fuel engine. *Energy* **2024**, *309*, 133164. [CrossRef]
24. Shi, C.; Zhang, Z.; Wang, H.; Wang, J.; Cheng, T.; Zhang, L. Parametric analysis and optimization of the combustion process and pollutant performance for ammonia-diesel dual-fuel engines. *Energy* **2024**, *296*, 131171. [CrossRef]
25. Mi, S.; Wu, H.; Pei, X.; Liu, C.; Zheng, L.; Zhao, W.; Qian, Y.; Lu, X. Potential of ammonia energy fraction and diesel pilot-injection strategy on improving combustion and emission performance in an ammonia-diesel dual fuel engine. *Fuel* **2023**, *343*, 127889. [CrossRef]
26. Yang, Z.; Miao, X.; Zhao, Z.; Zheng, J.; Di, Y.; Sun, L. Numerical Analysis of the Effects of Combustion Chamber Geometry on the Performance of Ammonia–Dimethyl Ether Dual-Fuel Engines. *J. Energy Eng.* **2025**, *151*, 04025044. [CrossRef]
27. Han, Z.; Reitz, R.D. Turbulence Modeling of Internal Combustion Engines Using RNG κ-ε Models. *Combust. Sci. Technol.* **1995**, *106*, 267–295. [CrossRef]

28. Beale, J.; Reitz, R. Modeling spray atomization with the Kelvin-Helmholtz/Rayleigh-Taylor hybrid model. *At. Sprays* **1999**, *9*, 623–650. [CrossRef]
29. Amsden, A.A.; O'Rourke, P.J.; Butler, T.D. *KIVA-II: A Computer Program for Chemically Reactive Flows with Sprays*; Los Alamos National Lab. (LANL): Los Alamos, NM, USA, 1989.
30. Schmidt, D.; Rutland, C. A New Droplet Collision Algorithm. *J. Comput. Phys.* **2000**, *164*, 62–80. [CrossRef]
31. O'Rourke, P.J.; Amsden, A.J.S.T. A Spray/wall Interaction Submodel for the KIVA-3 Wall Film Model. In Proceedings of the SAE 2000 World Congress, Detroit, MI, USA, 6–9 March 2000; pp. 281–298.
32. Senecal, P.K.; Pomraning, E.; Richards, K.J.; Briggs, T.E.; Choi, C.Y.; McDavid, R.M.; Patterson, M.A. Multi-Dimensional Modeling of Direct-Injection Diesel Spray Liquid Length and Flame Lift-off Length using CFD and Parallel Detailed Chemistry. *SAE Trans.* **2003**, *112*, 1331–1351.
33. Yin, G.; Li, J.; Zhou, M.; Li, J.; Wang, C.; Hu, E.; Huang, Z. Experimental and kinetic study on laminar flame speeds of ammonia/dimethyl ether/air under high temperature and elevated pressure. *Combust. Flame* **2022**, *238*, 111915. [CrossRef]
34. Hashemi, H.; Christensen, J.M.; Glarborg, P. High-pressure pyrolysis and oxidation of DME and DME/CH4. *Combust. Flame* **2019**, *205*, 80–92. [CrossRef]
35. Zhang, X.; Moosakutty, S.P.; Rajan, R.P.; Younes, M.; Sarathy, S.M. Combustion chemistry of ammonia/hydrogen mixtures: Jet-stirred reactor measurements and comprehensive kinetic modeling. *Combust. Flame* **2021**, *234*, 111653. [CrossRef]
36. Singh, A.S.; Shawnam; Reddy, V.M.; Kumar, S. Experimental and chemical kinetic analysis of laminar burning velocity of ammonia/dimethyl ether/air mixture at elevated temperature and pressure using a reduced-updated skeletal reaction model. *J. Energy Inst.* **2026**, *124*, 102334. [CrossRef]
37. Jowkar, S.; Tu, Z.; Shen, X. Comparative numerical analysis of engine performance and emissions of ammonia dual-fuel combustion with dimethyl ether, diethyl ether, and polyoxymethylene dimethyl ethers in a heavy-duty engine. *Int. J. Hydrogen Energy* **2026**, *227*, 154646. [CrossRef]
38. Wang, Z.; Yang, C.; Zhang, F.; Cheng, X. Effects of diesel injector nozzle angle and split diesel injection strategy on combustion and emission characteristics of an ammonia/diesel dual-fuel engine. *Energy* **2024**, *307*, 132686. [CrossRef]
39. Senecal, P.K.; Richards, K.J.; Pomraning, E.; Yang, T.; Dai, M.Z.; McDavid, R.M.; Patterson, M.A.; Hou, S.; Shethaji, T. A New Parallel Cut-Cell Cartesian CFD Code for Rapid Grid Generation Applied to In-Cylinder Diesel Engine Simulations. In Proceedings of the SAE World Congress & Exhibition, Detroit, MI, USA, 16–19 April 2007.
40. Senecal, P.; Pomraning, E.; Richards, K.; Som, S. Grid-Convergent Spray Models for Internal Combustion Engine CFD Simulations. In Proceedings of the Internal Combustion Engine Division Fall Technical Conference, Vancouver, BC, Canada, 23–26 September 2012.
41. Singh Gautam, P.; Partap Singh, A.; Chand, S.; Sehgal, A. Combustion knocking intensity behavior analysis using wavelet approach and optimizing water-emulsified diesel fuel: Engine combustion, performance and emission analysis with novel surfactants. *Fuel* **2025**, *391*, 134656. [CrossRef]
42. Vavra, J.; Bohac, S.V.; Manofsky, L.; Lavoie, G.; Assanis, D. Knock In Various Combustion Modes in a Gasoline-Fueled Automotive Engine. *J. Eng. Gas. Turbines Power* **2012**, *134*, 082807. [CrossRef]
43. Dec, J.E. Advanced compression-ignition engines—Understanding the in-cylinder processes. *Proc. Combust. Inst.* **2009**, *32*, 2727–2742. [CrossRef]
44. Jin, Z.; Mi, S.; Zhou, D.; Zhu, J.; Schirru, A.; Zhao, W.; Qian, Y.; Lucchini, T.; Lu, X. Insights into the combustion characteristics, emission formation sources, and optimization strategy of an ammonia-diesel dual-fuel engine under high ammonia ratio conditions. *Appl. Energy* **2024**, *373*, 123894. [CrossRef]
45. Frassoldati, A.; D'Errico, G.; Lucchini, T.; Stagni, A.; Cuoci, A.; Faravelli, T.; Onorati, A.; Ranzi, E. Reduced kinetic mechanisms of diesel fuel surrogate for engine CFD simulations. *Combust. Flame* **2015**, *162*, 3991–4007. [CrossRef]
46. Perini, F.; Busch, S.; Kurtz, E.; Warey, A.; Peterson, R.C.; Reitz, R. Limitations of Sector Mesh Geometry and Initial Conditions to Model Flow and Mixture Formation in Direct-Injection Diesel Engines. In Proceedings of the SAE Technical Paper Series, Detroit, MI, USA, 9–11 April 2019.
47. Zuo, Q.; Chen, L.; Chen, W.; Zhu, G.; Wang, Z.; Ma, Y.; Shen, Z.; Lu, C. Performance analysis of ammonia energy ratio on an ammonia-diesel engine in different fuel supply modes. *Fuel* **2025**, *384*, 134038. [CrossRef]
48. Agarwal, A.K.; Mehra, S.; Valera, H.; Mukherjee, N.K.; Kumar, V.; Nene, D. Dimethyl ether fuel injection system development for a compression ignition engine for increasing the thermal efficiency and reducing emissions. *Energy Convers. Manag.* **2023**, *287*, 117067. [CrossRef]
49. Mukherjee, N.K.; Valera, H.; Unnithan, S.; Kumar, V.; Dhyani, V.; Mehra, S.; Tripathi, A.; Nene, D.; Agarwal, A.K. Feasibility study of novel DME fuel injection Equipment: Part 1- fuel injection strategies and spray characteristics. *Fuel* **2022**, *323*, 124333. [CrossRef]
50. Mathieu, O.; Petersen, E.L. Experimental and modeling study on the high-temperature oxidation of Ammonia and related NOx chemistry. *Combust. Flame* **2015**, *162*, 554–570. [CrossRef]

51. Lee, G.-W.; Shon, B.-H.; Yoo, J.-G.; Jung, J.-H.; Oh, K.-J. The influence of mixing between NH3 and NO for a De-NOx reaction in the SNCR process. *J. Ind. Eng. Chem.* **2008**, *14*, 457–467. [CrossRef]
52. Joo, J.M.; Lee, S.; Kwon, O.C. Effects of ammonia substitution on combustion stability limits and NOx emissions of premixed hydrogen–air flames. *Int. J. Hydrogen Energy* **2012**, *37*, 6933–6941. [CrossRef]
53. Duynslaegher, C.; Jeanmart, H.; Vandooren, J. Flame structure studies of premixed ammonia/hydrogen/oxygen/argon flames: Experimental and numerical investigation. *Proc. Combust. Inst.* **2009**, *32*, 1277–1284. [CrossRef]

Disclaimer/Publisher's Note: The statements, opinions and data contained in all publications are solely those of the individual author(s) and contributor(s) and not of MDPI and/or the editor(s). MDPI and/or the editor(s) disclaim responsibility for any injury to people or property resulting from any ideas, methods, instructions or products referred to in the content.